Accurate Numerical Solutions for Transonic Viscous Flow over Finite Wings

V. N. Vatsa*
NASA Langley Research Center, Hampton, Virginia

An explicit multistage Runge-Kutta type of time-stepping scheme is used to solve the three-dimensional, compressible, thin-layer Navier-Stokes equations. A finite-volume formulation is employed to facilitate treatment of complex grid topologies encountered in three-dimensional calculations. Convergence to steady state is expedited through the use of acceleration techniques. Further numerical efficiency is achieved through vectorization of the computer code. The accuracy of the overall scheme is evaluated by comparing the computed solutions with the experimental data for a finite wing under different test conditions in the transonic regime. A grid refinement study is conducted to estimate the grid requirements for adequate resolution of salient features of such flows.

Introduction

THE availability of a new generation of supercomputers has opened up the possibility of computing transonic viscous flows over realistic aircraft components. In the present effort, a multistage Runge-Kutta type of time-stepping scheme developed by Jameson et al.[1] is employed. This method has been shown to produce accurate solutions of the Euler equations in both two- and three-dimensional flows.[2-5] Recently, this scheme has been employed for computing two-dimensional viscous flows by Swanson and Turkel[6] and for computing three-dimensional viscous flows by Agarwal and Deese.[7] Aside from the fact that this numerical scheme has been demonstrated for a wide range of flow problems, it also has the following advantages. Because it is a finite-volume scheme, it is flexible in treating arbitrary geometries for a wide range of grid topologies. Also, it is found to be numerically efficient for obtaining steady-state solutions through the use of acceleration techniques such as local time stepping, enthalpy damping, and implicit residual averaging. Another highly desirable property is the decoupling of spatial and temporal differencing that renders the steady-state solutions independent of the Courant number. Finally, this scheme is highly vectorizable on vector processors such as the Cray XMP and VPS-32, thereby making it very efficient from a computational point of view.

The main objective of the present work is to obtain accurate solutions for turbulent viscous flows over finite wings at high Reynolds number (Re) in the transonic flow regime. This is somewhat in contrast with the earlier works of Refs. 7 and 8, where the intent was to demonstrate the applicability of Jameson's scheme to three-dimensional viscous flows. Therefore, rather coarse grids were employed. In the present work, we assess the effects of grid refinement on the overall flow structure and establish guidelines regarding the minimum grid requirements for computing such flow problems.

Governing Equations

The basic equations under consideration here are the unsteady Navier-Stokes equations. These are specialized to a body-fitted coordinate system (ξ,η,ζ), where the η-coordinate lines are nearly orthogonal to the body surface. Since the dominant viscous effects at high Reynolds number turbulent flow arise from viscous diffusion normal to the body surface, a thin-layer assumption is employed, where only the viscous diffusion terms normal to the body surface are retained. The governing equations for a coordinate system fixed in time can then be written in the conservation law form as[9,10]

$$\frac{\partial \tilde{U}}{\partial t}+\frac{\partial \tilde{F}}{\partial \xi}+\frac{\partial \tilde{G}}{\partial \eta}+\frac{\partial \tilde{H}}{\partial \zeta}=\frac{\partial \tilde{S}}{\partial \eta} \tag{1}$$

where

$$\tilde{U}=J^{-1}U=J^{-1}\begin{bmatrix}\rho\\ \rho u\\ \rho v\\ \rho w\\ \rho E\end{bmatrix} \tag{2}$$

$$\tilde{F}=J^{-1}\begin{bmatrix}\rho\tilde{u}\\ \rho\tilde{u}u+\xi_x p\\ \rho\tilde{u}v+\xi_y p\\ \rho\tilde{u}w+\xi_z p\\ \rho\tilde{u}H\end{bmatrix} \tag{3a}$$

$$\tilde{G}=J^{-1}\begin{bmatrix}\rho\tilde{v}\\ \rho\tilde{v}u+\eta_x p\\ \rho\tilde{v}v+\eta_y p\\ \rho\tilde{v}w+\eta_z p\\ \rho\tilde{v}H\end{bmatrix} \tag{3b}$$

$$\tilde{H}=J^{-1}\begin{bmatrix}\rho\tilde{w}\\ \rho\tilde{w}u+\zeta_x p\\ \rho\tilde{w}v+\zeta_y p\\ \rho\tilde{w}w+\zeta_z p\\ \rho\tilde{w}H\end{bmatrix} \tag{3c}$$

Presented as Paper 86-1052 at the AIAA/ASME 4th Fluid Mechanics, Plasma Dynamics and Lasers Conference, May 12-14, 1986, Atlanta, GA; received June 22, 1986; revision received Dec. 9, 1986.

*Senior Research Scientist, Theoretical Aerodynamics Branch. Member AIAA.

$$\bar{S}=J^{-1}\begin{bmatrix} 0 \\ \mu\bar{\epsilon}(\eta_x^2+\eta_y^2+\eta_z^2)u_\eta+\frac{\mu\bar{\epsilon}}{3}(\eta_x u_\eta+\eta_y v_\eta+\eta_z w_\eta)\eta_x \\ \mu\bar{\epsilon}(\eta_x^2+\eta_y^2+\eta_z^2)v_\eta+\frac{\mu\bar{\epsilon}}{3}(\eta_x u_\eta+\eta_y v_\eta+\eta_z w_\eta)\eta_y \\ \mu\bar{\epsilon}(\eta_x^2+\eta_y^2+\eta_z^2)w_\eta+\frac{\mu\bar{\epsilon}}{3}(\eta_x u_\eta+\eta_y v_\eta+\eta_z w_\eta)\eta_z \\ \left\{\begin{array}{l}\frac{\mu\bar{\epsilon}}{2}(\eta_x^2+\eta_y^2+\eta_z^2)(u^2+v^2+w^2)_\eta \\ +\frac{\mu\bar{\epsilon}}{3}(\eta_x u+\eta_y v+\eta_z w)(\eta_x u_\eta+\eta_y v_\eta+\eta_z w_\eta) \\ +\left(\frac{\gamma}{\gamma-1}\right)\frac{\mu\bar{\epsilon}}{\sigma}(\eta_x^2+\eta_y^2+\eta_z^2)T_\eta\end{array}\right\}\end{bmatrix} \tag{3d}$$

$$\tilde{S}=\sqrt{\gamma}\,\frac{M_\infty}{R_{e_\infty}}\cdot\bar{S} \tag{3e}$$

The contravariant velocity components used in Eqs. (3a–3d) are defined as

$$\begin{aligned}\tilde{u}&=\xi_x u+\xi_y v+\xi_z w\\ \tilde{v}&=\eta_x u+\eta_y v+\eta_z w\\ \tilde{w}&=\zeta_x u+\zeta_y v+\zeta_z w\end{aligned} \tag{4}$$

The transformation metrics are defined as

$$\begin{aligned}\xi_x&=J(y_\eta z_\zeta-y_\zeta z_\eta) & \zeta_y&=J(x_\eta z_\xi-x_\xi z_\eta)\\ \eta_x&=J(y_\zeta z_\xi-y_\xi z_\zeta) & \xi_z&=J(x_\eta y_\zeta-x_\zeta y_\eta)\\ \zeta_x&=J(y_\xi z_\eta-y_\eta z_\xi) & \eta_z&=J(x_\zeta y_\xi-x_\xi y_\zeta)\\ \xi_y&=J(x_\zeta z_\eta-x_\eta z_\zeta) & \zeta_z&=J(x_\xi y_\eta-x_\eta y_\xi)\\ \eta_y&=J(x_\xi z_\zeta-x_\zeta z_\xi)\end{aligned} \tag{5}$$

where J is the Jacobian of transformation given by

$$J^{-1}=x_\xi(y_\eta z_\zeta-y_\zeta z_\eta)-y_\xi(x_\eta z_\zeta-x_\zeta z_\eta)+z_\xi(x_\eta y_\zeta-y_\eta x_\zeta) \tag{6}$$

In the preceding set of equations, distances have been nondimensionalized by a reference length L, usually taken to be the semispan of the wing; density, pressure, and viscosity by their respective freestream values; and velocities by a reference velocity $u_{\text{ref}}=a_\infty/\sqrt{\gamma}$, where a_∞ is the freestream speed of sound; and enthalpy by u_{ref}^2. For an ideal gas, the enthalpy is then given by the relation

$$\rho H=\left(\frac{\gamma}{\gamma-1}\right)p+\rho\left(\frac{u^2+v^2+w^2}{2}\right) \tag{7}$$

In the governing equations presented here, the effect of turbulence is accounted for through the concepts of an eddy viscosity and eddy conductivity. In the momentum equations, the molecular viscosity μ is replaced by effective viscosity μ_e,

$$\mu_e=\mu+\mu_t=\mu(1+\mu_t/\mu)=\mu\bar{\epsilon} \tag{8a}$$

where

$$\bar{\epsilon}=1+\mu_t/\mu \tag{8b}$$

Here μ_e is the effective viscosity and μ_t the turbulent viscosity. Similarly, in the energy equation, the molecular conductivity k is replaced by the effective conductivity k_e,

$$\begin{aligned}k_e&=k+k_t=\frac{C_p}{\sigma}\mu+\frac{C_p}{\sigma_t}\mu_t\\ &=\frac{C_p\mu}{\sigma}\left(1+\frac{\sigma}{\sigma_t}\frac{\mu_t}{\mu}\right)=\frac{C_p\mu}{\sigma}\tilde{\epsilon}=k\tilde{\epsilon}\end{aligned} \tag{9a}$$

where

$$\tilde{\epsilon}=1+\frac{\sigma}{\sigma_t}\frac{\mu_t}{\mu} \tag{9b}$$

where σ is the laminar Prandtl number and σ_t the turbulent Prandtl number. In the present work, we have used the algebraic turbulence model of Baldwin and Lomax[9] to evaluate the turbulence quantities. Note that wake turbulence modeling is included in this formulation of the turbulence model.[9]

Finite-Volume Formulation

The governing equations, while written in generalized curvilinear coordinates, are used here in a finite-volume formulation. In a recent paper, Thompkins[11] has shown that the finite-difference solution to the fluid dynamic equations in strong conservation form in a transformed space is equivalent to the solution of a flux-summation algorithm in physical space or the finite-volume algorithm, subjected to proper interpretation of the metric derivatives. Traditionally, the metric derivatives in a finite-difference formulation are evaluated using central difference formulas. In the present scheme, however, the ratio of the metric derivatives to the Jacobian is taken to be the appropriate projected area of cell faces and the reciprocal of the Jacobians is taken to be the cell volumes. For example, ξ_x/J is computed as the area of a cell-face at fixed ξ location projected onto the x axis and so on. Such an approach then honors the geometric conservation law and makes the numerical scheme compatible with the finite-volume formulation. One can then write the governing equations in the semidiscrete form as

$$\frac{\mathrm{d}}{\mathrm{d}t}(\tilde{U})+(\tilde{F}_{i+\frac{1}{2},j,k}-\tilde{F}_{i-\frac{1}{2},j,k})+(\tilde{G}_{i,j+\frac{1}{2},k}-\tilde{G}_{i,j-\frac{1}{2},k})+(\tilde{H}_{i,j,k+\frac{1}{2}}-\tilde{H}_{i,j,k-\frac{1}{2}})=(\tilde{S}_{i,j+\frac{1}{2},k}-\tilde{S}_{i,j-\frac{1}{2},k}) \tag{10}$$

where

$$\begin{aligned}\tilde{F}_{i\pm\frac{1}{2},j,k}&=\tfrac{1}{2}(\tilde{F}_{i,j,k}+\tilde{F}_{i\pm1,j,k})\\ \tilde{G}_{i,j\pm\frac{1}{2},k}&=\tfrac{1}{2}(\tilde{G}_{i,j,k}+\tilde{G}_{i,j\pm1,k})\\ \tilde{H}_{i,j,k\pm\frac{1}{2}}&=\tfrac{1}{2}(\tilde{H}_{i,j,k}+\tilde{H}_{i,j,k\pm1})\end{aligned} \tag{11}$$

Let us now describe the manner in which the viscous fluxes are evaluated. Notice that a typical viscous flux term is of the form $\sum_n C^n(\partial f^n/\partial\eta)$, where C^n consists of a grouping of flow variable and metric derivatives and $\partial f^n/\partial\eta$ represents first difference of a flow variable. The total viscous flux contains n terms and hence, the summation. We can discretize the viscous fluxes in the following manner

$$\begin{aligned}\tilde{S}_{i,j+\frac{1}{2},k}&=\sum_n C^n_{i,j+\frac{1}{2},k}(f^n_{i,j+1,k}-f^n_{i,j,k})\\ \tilde{S}_{i,j-\frac{1}{2},k}&=\sum_n C^n_{i,j-\frac{1}{2},k}(f^n_{i,j,k}-f^n_{i,j-1,k})\end{aligned} \tag{12}$$

where

$$C^n_{i,j\pm\frac{1}{2},k} = \frac{1}{2}(C^n_{i,j,k} + C^n_{i,j\pm1,k}) \tag{13}$$

Let us write the flux terms in operator notation

$$\frac{\mathrm{d}}{\mathrm{d}t}(J^{-1}U) + Q(U) = 0 \tag{14}$$

where Q contains all the convective and viscous fluxes.

In order to suppress any odd-even point decoupling in the numerical solution and to prevent the appearance of oscillations in the vicinity of shock waves and stagnation points, artificial dissipation terms are added to the finite-volume scheme. Equation (14) is thus replaced by

$$\frac{\mathrm{d}}{\mathrm{d}t}(J^{-1}U) + Q(U) - D(U) = 0 \tag{15}$$

where $D(U)$ represents the added dissipative terms. We use the form of artificial dissipation devised by Jameson et al.,[1] where a blend of second and fourth differences with coefficients depending on the local pressure gradients are employed. Details of constructing the dissipative terms are readily available[1,6,7] and are therefore not presented here.

Time-Stepping Scheme

A multistage Runge-Kutta scheme is employed to advance solution of Eq. (15) in time. To advance the solution from time level n to $n+1$ using four stages, the scheme takes the following form:

$$U^{(0)} = U^{(n)}$$

$$U^{(1)} = U^{(0)} - \frac{\Delta t}{4} R(U^{(0)})$$

$$U^{(2)} = U^{(0)} - \frac{\Delta t}{3} R(U^{(1)})$$

$$U^{(3)} = U^{(0)} - \frac{\Delta t}{2} R(U^{(2)})$$

$$U^{(n+1)} = U^{(0)} - \Delta t R(U^{(3)}) \tag{16}$$

where

$$R(U^{(q)}) = J[Q(U^{(q)}) - D(U^{(q)})] \tag{17}$$

The scheme of Eq. (16) is a modified form of the classical Runge-Kutta scheme and is very attractive for three-dimensional problems, since it requires only two time levels of the solution vector in memory. Jameson and Baker[4] have indicated that this modified scheme is fourth-order accurate in time for linear problems; whereas, Swanson and Turkel[6] have pointed out that it is second-order accurate in time for nonlinear problems. Since our primary objective here is to obtain steady-state solutions in the most efficient manner, second-order accuracy in time is considered adequate. The Runge-Kutta time marching scheme described here is shown to be more efficient than an unsplit MacCormack scheme.[1] In addition, due to the decoupling of spatial and temporal discretizations, the steady-state solution is independent of the time step. This scheme is therefore amenable to acceleration techniques to enhance convergence to steady-state solution.

Acceleration Techniques

The modified Runge-Kutta scheme described here has a CFL (Courant-Friedricks-Lewy) number limit of $2\sqrt{2}$ for purely hyperbolic one-dimensional problems. For three-dimensional viscous flow problems, the CFL number is somewhat lower due to the presence of large cell aspect ratios and viscous dissipation. Three techniques (namely, local time stepping, enthalpy damping, and residual smoothing) are employed here to enhance the convergence to a steady-state solution. Local time stepping is implemented by using the maximum local time step Δt, based on the stability limit, in every cell to advance the solution in time. This results in the use of much larger values of Δt than permitted by the global minimum value of Δt. This allows faster signal propagation and, hence, faster convergence. The second technique for improving steady-state convergence, known as enthalpy damping, was introduced by Jameson et al.[1] for the Euler equations. Basically, artificial damping terms proportional to the deviation of the toal enthalpy from its steady-state freestream value are added to the governing equations. This provides additional damping, especially through the initial transients, and improves the overall convergence to the steady-state solution. It was pointed out by Swanson and Turkel[6] that enthalpy damping can be used for adiabatic turbulent viscous flows with unit Prandtl number, without compromising the accuracy of the solutions. Note that enthalpy damping can be used as a preconditioner in the transient stage and, thus, problems with heat transfer can also be solved.

The final technique for improving convergence is based on a residual smoothing technique devised by Lerat[12] for the Lax-Wendroff scheme and by Jameson[13] for the Runge-Kutta scheme. As suggested by Jameson and Baker,[4] the residual smoothing for three-dimensional flows is applied to the residual in the product form

$$(1-\epsilon_\xi\delta^2_\xi)(1-\epsilon_\eta\delta^2_\eta)(1-\epsilon_\zeta\delta^2_\zeta)\bar{R}_{i,j,k} = R_{i,j,k} \tag{18}$$

where $R_{i,j,k}$ represents the original residuals from the explicit scheme and $\bar{R}_{i,j,k}$ represents the residuals after a sequence of smoothings in the three coordinate directions is applied. In Eq. (18), $\epsilon_\xi, \epsilon_\eta, \epsilon_\zeta$ are the smoothing parameters in the ξ, η, ζ directions, respectively, and δ is the central difference operator. Due to the factored form of Eq. (18), it is necessary only to solve a sequence of tridiagonal equations for separate scaler variables. Based on linear stability analysis, Jameson and Baker[4] concluded that the Runge-Kutta scheme with residual smoothing is unconditionally stable if the smoothing parameter is chosen to be sufficiently large. In practice, however, very large values of the CFL number do not necessarily result in the fastest convergence to the steady-state solution. Swanson and Turkel[6] came to a similar conclusion based on analysis of residual smoothing in conjunction with a two-stage Runge-Kutta scheme. Thus, the optimum value of CFL number and the smoothing parameters must be determined. The mesh stretching in each coordinate direction is an important factor in this process. Generally speaking, the higher the mesh stretching rate along a coordinate direction, the larger the value of ϵ required in that direction for residual smoothing to perform well. We have conducted numerical experiments to determine the value of these parameters for solving high Reynolds number, turbulent, viscous flow over an isolated wing at several test conditions. Based on this exercise, the following combination of parameters was found to work quite well: CFL number $=4.5$, $\epsilon_\xi = 0.4$, $\epsilon_\eta = 0.8$, and $\epsilon_\zeta = 0.4$. We would like to point out that this is not necessarily an optimum choice; however, it may provide a good starting point for high Reynolds number, transonic, turbulent, viscous flow problems.

Boundary Conditions

A typical domain for the three-dimensional viscous flow problem consists of several different types of boundaries requiring appropriate boundary condition treatments. For a symmetric isolated wing problem investigated here, the

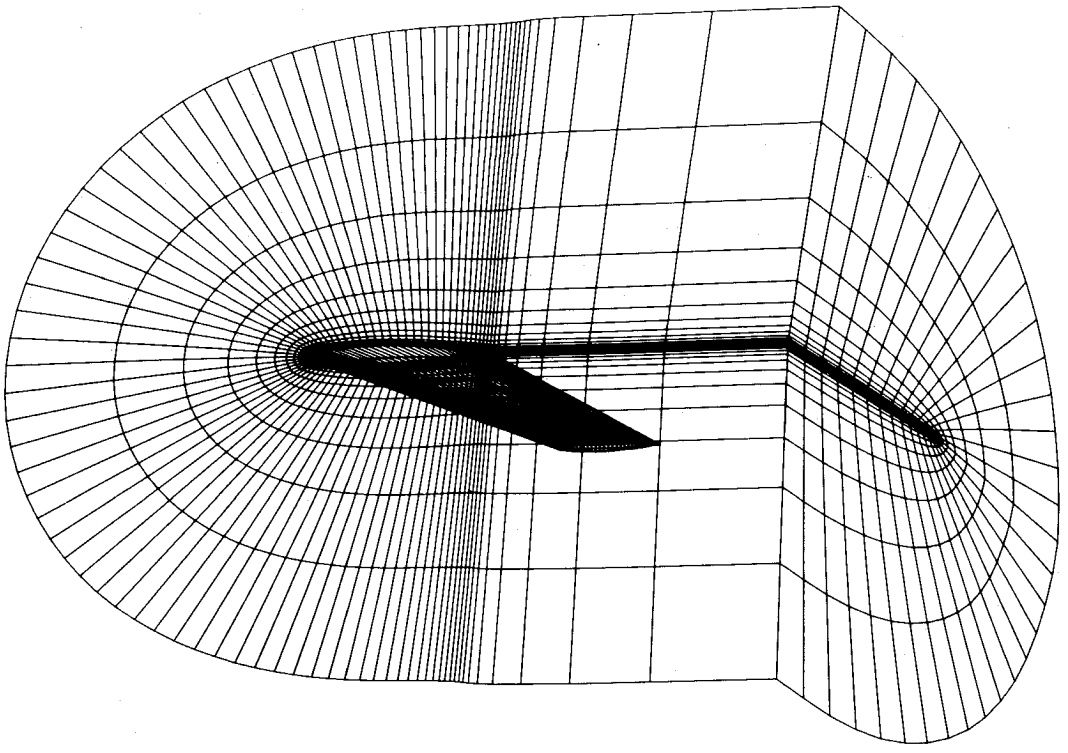

Fig. 1 Partial view of C-O grid for ONERA M6 wing calculation.

following boundaries must be considered: a solid wall at the body surface, the far field away from the body surface, the downstream plane in the wake region, and the symmetry plane at the root section. At the body surface, no-slip and zero-injection conditions are imposed by setting $u=v=w=0$. For temperature, an adiabatic condition is employed and normal pressure gradient at the body surface is set equal to zero. The treatment of the far-field boundary condition is based on the Riemann invariants for one-dimensional flow normal to the far-field boundary as discussed in detail by Jameson and Baker[4] and Thomas and Salas.[14] At the downstream plane in the wake region, a zero-order extrapolation is used for all the variables. Symmetry conditions are used at the root section plane on all the variables except for the cross flow velocity component w, which is taken to be antisymmetric.

Grid Generation and Topology

The grid topology for a given problem should be selected carefully based on its ability to model the physical configuration accurately and use the mesh points efficiently. Eriksson[15] has compared relative efficiencies of different mesh topologies for resolving inviscid (Euler) flow over finite wings and concluded that the O-O topology gives the best resolution on the wing surface for a given number of mesh points. For viscous flow problems, it is preferable to use C-grids along chordwise sections for accurate resolution of the wake flow developing downstream of the trailing edge. For the spanwise direction, O-type meshes are considered here giving rise to a C-O topology. The C-O grids employed in the present calculations were generated by using a transfinite interpolation technique similar to the one developed by Eriksson.[15] This is a very powerful technique, since it can be used for controlling both the normal spacing and the direction of the coordinate lines leaving the boundary surface through careful choice of blending functions. Thus, we are able to generate boundary-fitted meshes where one set of coordinate lines is nearly orthogonal to the surface and has adequate spacing in the viscous layer to accurately resolve the high Reynolds number turbulent flow. A typical mesh generated using this procedure is shown in Fig. 1, where grid clustering in leading- and trailing-edge regions and in the viscous region near the wing surface is clearly visible.

Results and Discussion

The main emphasis in this paper is on obtaining accurate solutions for an isolated wing. The M6 ONERA wing for which extensive pressure data[16] are available over a wide range of Mach numbers (M_∞) and angles of attack (α) is selected to be the basic test configuration. A mesh refinement study is conducted for both the subcritical and supercritical cases to provide estimates of grid requirement for accurate resolution of such flows. In order to ascertain convergence, all calculations were run until at least four orders of magnitude reductions were observed in the residuals which took between 1000–3000 time cycles for the cases investigated here. Results for three test conditions are presented here: 1) subcritical case ($M_\infty=0.699$, $\alpha=3.06$ deg); 2) supercritical case at low angle of attack ($M_\infty=0.84$, $\alpha=3.06$ deg); and 3) supercritical case at high angle of attack ($M_\infty=0.84$, $\alpha=6.06$ deg). The Reynolds number based on freestream conditions and the mean aerodynamic chord is 11.7×10^6. Since there is no available information on wind-tunnel interference effects, the present calculations are run at the geometric angle of attack stated in Ref. 16. All the calculations presented here were run by assuming the flow to be fully turbulent on the entire wing.

Subcritical Case

The first set of results presented here corresponds to the subcritical flow conditions at $M_\infty=0.699$ and $\alpha=3.06$ deg. The initial calculations were performed on a C-O grid of $97\times49\times17$ (streamwise, normal, and spanwise directions) node points. A partial view of this mesh in the near field is shown in Fig. 1, where every other point is plotted in the normal direction for clarity. In this figure, one can see the grid distribution on the wing surface, root section, and a downstream plane in the wake region. Grid clustering in the wing leading- and trailing-edge regions and in the thin viscous layer adjacent to the wing surface is clearly visible. Note that this is only a partial view of the near-field grid—the actual far-field boundaries are placed at a distance of approximately 15 root chords away from the wing. The computed pressure distributions on this mesh are compared with the experimental data in Fig. 2 at three spanwise locations, $\zeta=0.44$, 0.65, and 0.90 where ζ is the spanwise distance normalized with semispan. Although the computed

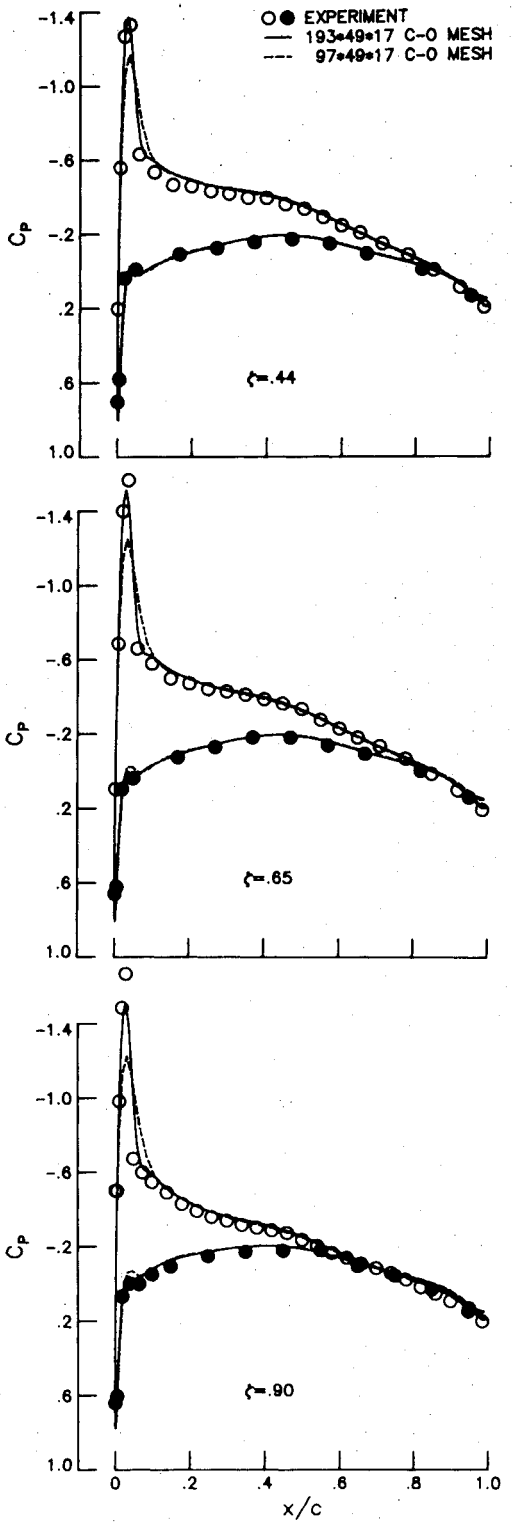

Fig. 2 Effect of streamwise grid refinement ($M_\infty = 0.699$, $\alpha = 3.06$ deg).

solutions display the overall characteristics observed experimentally, the quantitative agreement with data in the leading-edge region on the upper surface where very sharp suction peaks exist is poor. The calculations were then repeated on a mesh with $193 \times 49 \times 17$ grid points, which has twice as many points in the streamwise direction as the first mesh. These results are also shown in Fig. 2 and compare quite well with the data even at the outboard stations of the wing. No further grid refinement was deemed warranted in light of these comparisons for this case. It should also be mentioned that the effects of grid refinement in the normal direction are not presented here, but that such an exercise was conducted in the earlier phases of this work. Based on that experience, the normal mesh distribution was selected such that further grid refinement had very minimal effect on the pressure distribution.

Supercritical Case: Attached Flow

For the next test case, we have selected the supercritical flow at $M_\infty = 0.84$ and $\alpha = 3.06$ deg, which is one of the most standard test cases investigated by earlier researchers. Most of the work presented earlier for this test case is based on inviscid equations. A systematic grid refinement study is conducted to provide quantitative estimates of the effect of streamwise and spanwise spacing on the computed solutions.

The first set of calculations for this case was performed on a $97 \times 49 \times 17$ grid and the computed pressure distributions are compared with the experimental data at three spanwise locations in Fig. 3a. From these results, it appears that the streamwise resolution is inadequate to accurately resolve the sharp suction peaks in the leading-edge region. Also, the predicted shocks appear very smeared when compared to the data. To assess the effect of streamwise resolution, the next set of calculations was performed on a $193 \times 49 \times 17$ mesh, the solutions of which are also plotted in Fig. 3a. A significant improvement is observed in the predicted pressure distributions in the leading-edge region. However, the shock definition from the computed results is still not satisfactory. Recall that the agreement of computed results with experimental data for the subcritical case on the same mesh was excellent. This is attributed to the existence of a λ shock on the wing surface under supercritical conditions, which is formed when the double shock on the inboard stations merges into a single (much stronger) shock toward the outboard stations on the wing. Thus, much stronger gradients are present in the spanwise direction under supercritical conditions. To resolve such spanwise variations, the number of mesh points was doubled in the spanwise direction and the final solutions for this case were thus run on a $193 \times 49 \times 33$ grid. These solutions are presented in Fig. 3b along with solutions obtained on a $193 \times 49 \times 17$ grid and compare quite well with the experimental data. The computed shocks with finer spanwise mesh are fairly sharp and their locations are well predicted. It is clear from these comparisons that adequate spanwise resolution is just as important as the streamwise resolution for accurate prediction of supercritical flows.

Supercritical Case with Separated Flow

The final test case selected for presentation here corresponds to $M_\infty = 0.84$ and $\alpha = 6.06$ deg. This test case has been selected to assess the accuracy of thin-layer Navier-Stokes (TLNS) solutions under more severe flow conditions. Much stronger shocks develop under these test conditions on the upper surface of the wing, resulting in significant flow separation. A mesh consisting of $193 \times 65 \times 33$ points is employed for the viscous flow calculations. Based on the mesh refinement study described above, this mesh should provide adequate resolution of important features of the flow. The number of mesh points in the normal direction has been increased (compared to the attached flow cases) to resolve the thicker boundary layer developing in the separated flow regions. A total of 3000 iterations (time cycles) was run for this case and the convergence history is shown in Fig. 4.

In Fig. 4, the solid line represents the log of residual for continuity equation normalized by its starting value; the dashed line represents the number of supersonic points normalized by its final value. Note from this figure that the number of supersonic points converged approximately in 1800 cycles and that the residual converged to better than four orders in 3000 iterations. This is considered to be very encouraging in view of the extremely fine mesh ($\Delta y_{\min} \simeq 10^{-5}$ chords with a total of 413,985 grid points) employed in these

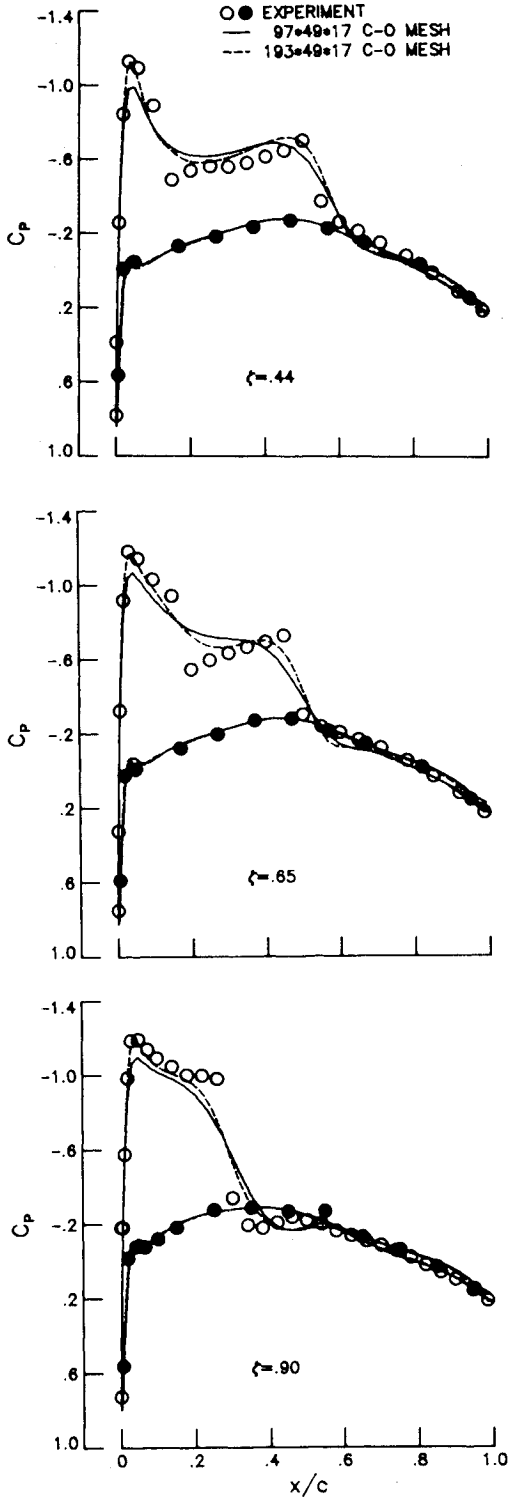

Fig. 3a Effect of streamwise grid refinement ($M_\infty = 0.84$, $\alpha = 3.06$ deg).

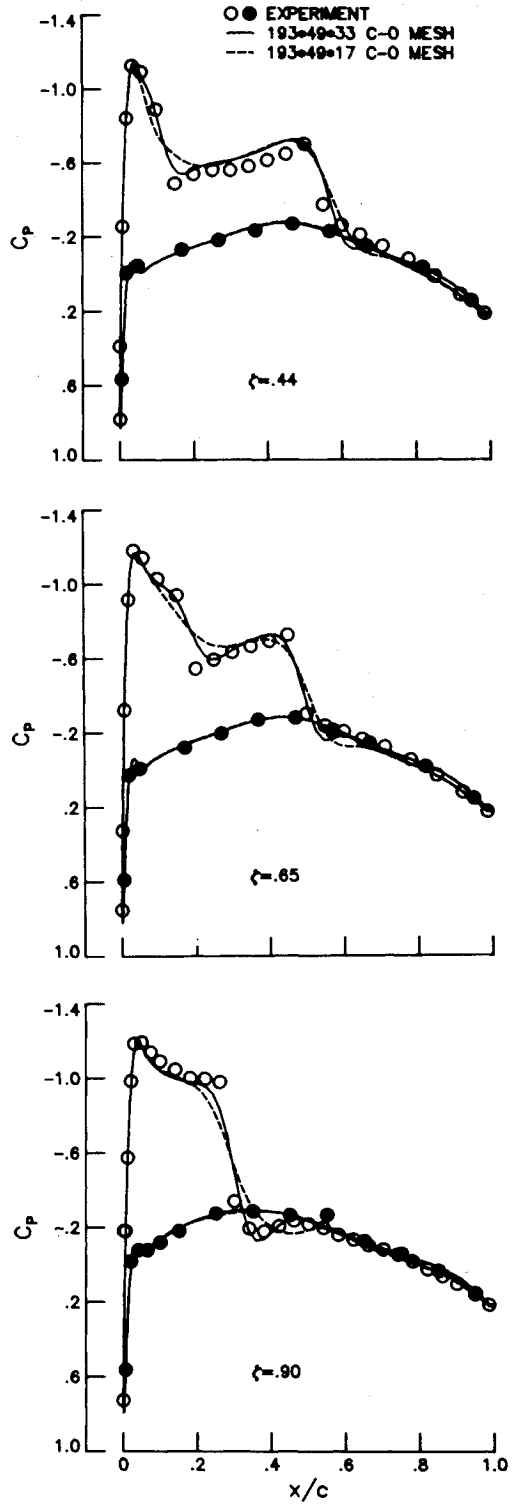

Fig. 3b Effect of spanwise grid refinement ($M_\infty = 0.84$, $\alpha = 3.06$ deg).

calculations. Although we have not shown the convergence histories of the cases studied in the previous sections, it is worth mentioning that similar levels of convergence were obtained in about half as many iterations or less, depending on the number of mesh points. Obviously, the coarser the mesh, the less iterations it takes to reach the steady-state solution. The present vectorized version of the code takes approximately 1.6×10^{-5} CPU s/grid point/iteration on NASA Langley's VPS-32 computer system. Thus, most of the cases presented here converged in less than two hours of computer time.

To get a visual picture of the flowfield on the upper surface of the wing, particle traces confined to remain on the wing surface are computed and shown in Fig. 5. The separation and attachment lines have also been marked. It is observed from this figure that a significant reverse flow region exists on the outboard section of the wing. The flow separates due to strong adverse pressure gradients across strong shocks and then reattaches downstream due to a decrease in the magnitude of adverse pressure gradient. A very small region of trailing-edge separation is also visible in this figure.

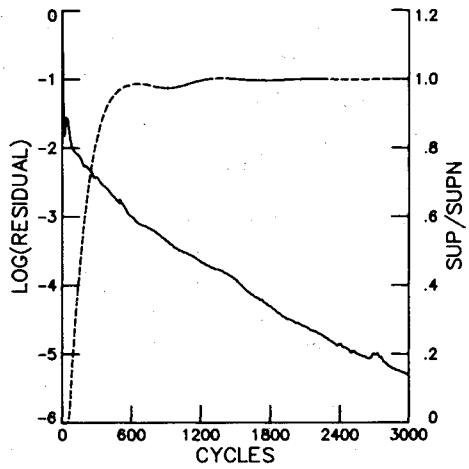

Fig. 4 Convergence history for separated flow case ($M_\infty = 0.84$, $\alpha = 6.06$ deg).

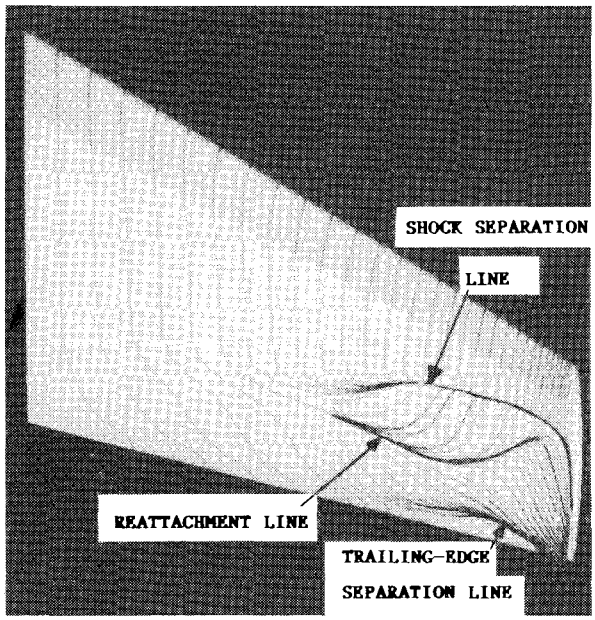

Fig. 5 Surface streamline pattern for separated flow case ($M_\infty = 0.84$, $\alpha = 6.06$ deg).

Let us now look at the computed pressure distributions. To assess the viscous effects, inviscid (Euler) solutions were obtained on a $193 \times 33 \times 33$ mesh, keeping the surface mesh distribution identical to the one used for viscous TLNS calculations. The computed results are shown in Fig. 6 at $\zeta = 0.44$, 0.65, and 0.90. It is observed from this figure that the inviscid solutions on the upper surface are in significant error all the way from the inboard to outboard stations. The shock position predicted by the inviscid solutions is up to 20% chord downstream of the experimentally observed location. There is also a considerable overshoot in the pressures at the foot of the shock. The viscous calculations for this case indicate a sizeable reverse flow region on the upper surface of the wing (see Fig. 5) resulting in the significant boundary-layer growth. Due to the thickening of the boundary layer (and, hence, the displacement body), the shock moves forward. Also, the pressure tends to plateau in the reverse flow region behind the shock. This combined with the forward movement of the shock brings the viscous pressure distributions closer to the experimental data. Although the viscous solutions are much closer to the experimental data than the inviscid solutions, the agreement is not quite as good as that observed for the attached flow

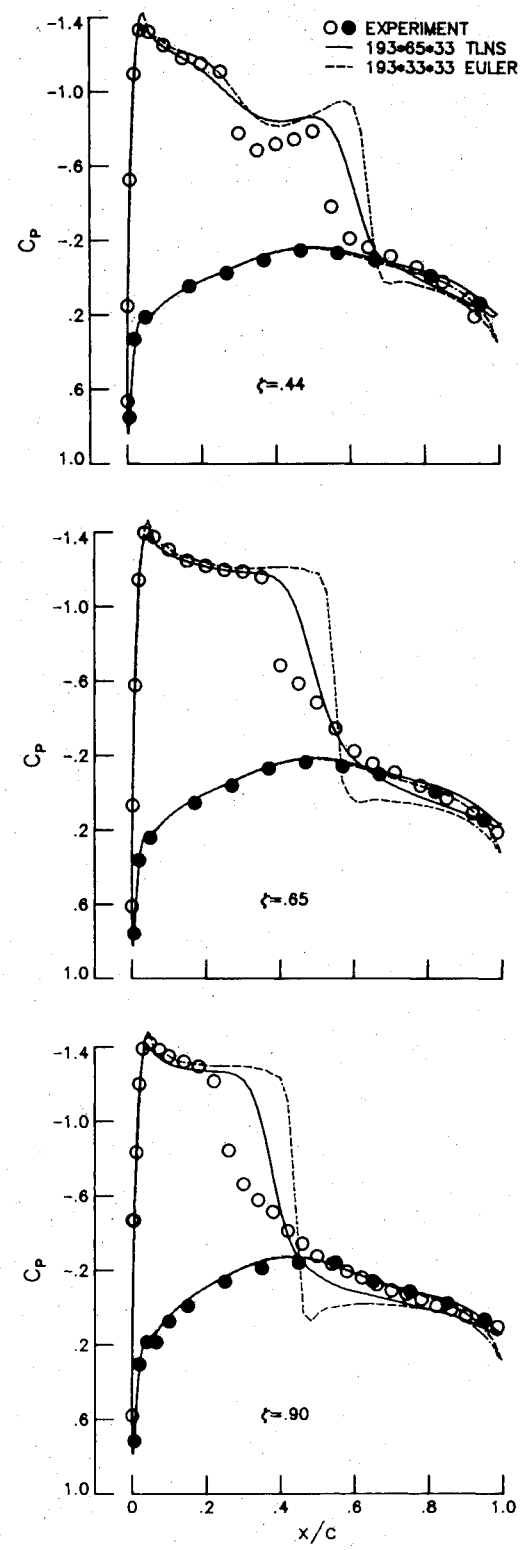

Fig. 6 Comparison of viscous and inviscid solutions for separated flow case ($M_\infty = 0.84$, $\alpha = 6.06$ deg).

cases investigated earlier. These results are, however, considered to be very encouraging, keeping in mind that an algebraic equilibrium turbulence model, namely, the Baldwin-Lomax model, has been employed in these calculations. The limitations of such turbulence models in computing separated flows is well known and has led to several modifications[17,18] in the past. Findings based on the relaxation model of Shang and Hankey[17] will be presented in the next section.

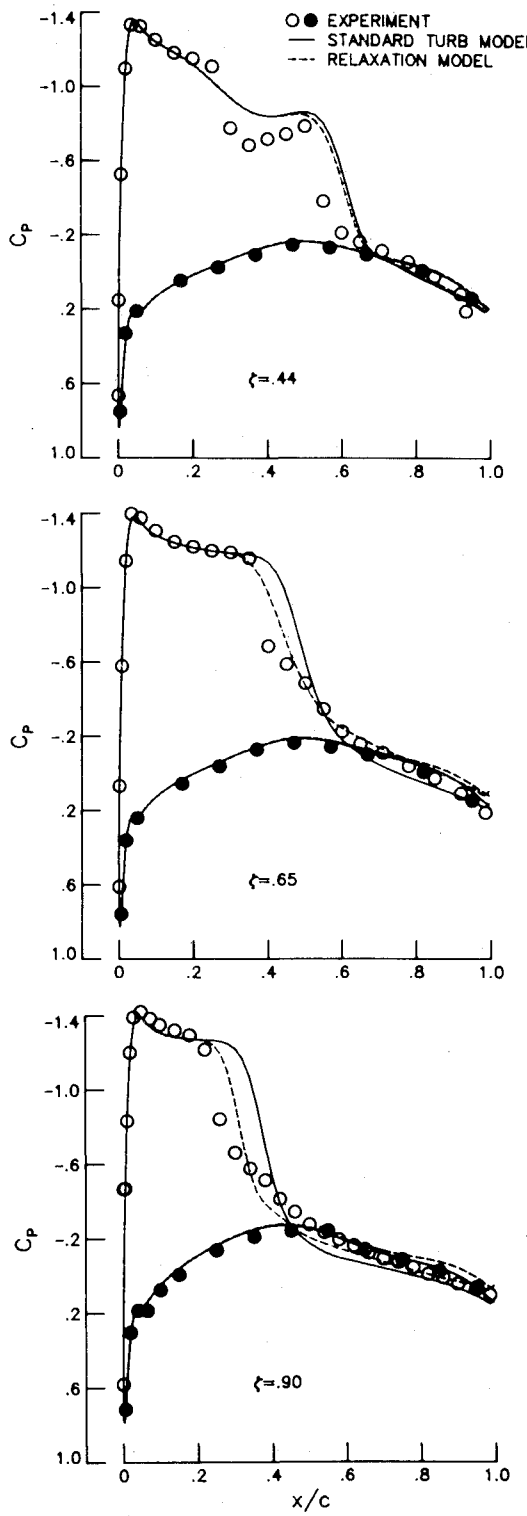

Fig. 7 Effect of relaxation turbulence model on separated flow case ($M_\infty = 0.84$, $\alpha = 6.06$ deg).

Effect of Turbulence Model

Based on the results presented in the previous section, it was concluded that the basic equilibrium turbulence model underpredicts the extent of reverse flow region and hence results in poor agreement with data in the vicinity of shocks. Shang and Hankey[17] made similar observations while studying separated flows in a compression corner and formulated a relaxation turbulence model to resolve this dilemma. The basic concept involved including the history effects into the turbulence model in separated flow regions (strong interaction zone) to reflect the physics of the problem more accurately. This was accomplished by modifying the eddy viscosity in the strong interaction zone as follows:

$$\bar{\epsilon} = \bar{\epsilon}_{\text{upstream}} + (\bar{\epsilon}_{\text{equil}} - \bar{\epsilon}_{\text{upstream}})[1 - \exp(-\Delta x/\lambda)] \qquad (19)$$

where $\bar{\epsilon}_{\text{upstream}}$ is the value of eddy viscosity at an initial location where strong interaction is initiated and $\bar{\epsilon}_{\text{equil}}$ the local value of eddy viscosity computed by using the standard equilibrium model. In Eq. (19), Δx denotes the distance between these two locations and λ the relaxation length. Shang and Hankey[17] suggested a value of $10\delta_0$ for the relaxation length λ, where δ_0 is boundary-layer thickness at the upstream station where strong interaction is initiated. In their investigation on the study of separated flows, Visbal and Knight[18] obtained good data correlation by employing a value of δ_0 for the relaxation length in conjunction with the Baldwin-Lomax model. As conjectured by Visbal and Knight, the relaxation length depends on the separation to reattachment length. Thus, the larger the separation to reattachment length, the larger the relaxation length and vice versa. Using this as a starting point, it was decided to relate the relaxation length λ directly to the separation to reattachment length or to the separation extent as

$$\lambda = c(x_{\text{reattach}} - x_{\text{sep}}) \qquad (20)$$

where c is a constant taken to be 0.25, making the relaxation length comparable to the one employed by Visbal and Knight.[18] It is hoped that such a formulation will be more universal in nature, since the relaxation length is based on the actual extent of separation rather than on the boundary-layer properties in the upstream region. It should be mentioned here that the relaxation model described in Eqs. (19) and (20) is implemented at a given spanwise station in the stripwise manner. Thus, separation and reattachment locations used in the relaxation model are determined by assuming the flow to be locally two-dimensional. Finally, the $\bar{\epsilon}_{\text{upstream}}$ for a given spanwise station is taken to be value of eddy viscosity evaluated from the standard Baldwin-Lomax turbulence model (equilibrium model) along the coordinate line emanating from a mesh point just upstream of the separation point.

The TLNS solutions obtained with this relaxation model are shown in Fig. 7 along with the experimental data. The convergence properties of the algorithm deteriorated when this relaxation model was activated. It is believed that this may be due to the dynamic nature of this model as implemented here and work is continuing on improving its convergence properties. The results presented here should nonetheless serve as a good indication of the sensitivity of the viscous solutions to such modifications in turbulence models. In order to assess the effect of change in the turbulence model, the solutions from the standard turbulence model are also plotted in Fig. 7. Note that, as a consequence of the relaxation model, the predicted shock location on the outboard stations of the upper surface where reverse flow exists lies closer to the data and the overall agreement with the measured pressure distribution is significantly improved. It is thus clear that history effects must be included in the turbulence model for predicting flows with embedded reverse flow regions.

Conclusions

A finite-volume scheme for numerical integration of thin-layer Navier-Stokes (TLNS) equations has been presented for three-dimensional flows. The numerical procedure is based on a four-stage Runge-Kutta time-stepping scheme. Convergence to steady-state solution is enchanced through local time stepping, enthalpy damping and implicit residual smoothing. Further efficiency of the numerical algorithm is achieved through vectorization of the computer code.

Solutions have been obtained for high Reynolds number, turbulent, viscous flow past an isolated wing for several test conditions. A grid refinement study is conducted for estimating grid requirements for accurate resolution of salient features of the flow. The computed pressure distributions on fine meshes employed here compared quite well with the measured data for attached flows. For high angles of attack with flow separation, the agreement with the data is less satisfactory. This is attributed to the lack of upstream effects in an equilibrium turbulence model, such as the Baldwin-Lomax turbulence model employed here. An attempt is made to include upstream history in the turbulence model through a relaxation model. Preliminary calculations using the relaxation model are very encouraging. Further work should continue toward improving the turbulence model for separated flows to enhance the usefulness of the present scheme. Also, the effect of neglecting some of the diffusion terms in the TLNS equations should be assessed by comparing the present solutions with the solutions to full Navier-Stokes equations, particularly for the separated flow case, where thin-layer approximation would be most suspect.

Acknowledgments

The author would like to express his gratitude to Mr. Bruce Wedan for generating the C-O meshes used in the present computations. The author would also like to express his immense thanks to Drs. Charlie Swanson and Eli Turkel for many useful discussions on various aspects of the numerical scheme employed here. Finally, the encouragement provided by Messrs. Jerry South and Manny Salas during the entire course of this investigation is greatly appreciated.

References

[1]Jameson, A., Schmidt, W., and Turkel, E., "Numerical Solutions of the Euler Equations by Finite Volume Methods Using Runge-Kutta Time-Stepping Schemes," AIAA Paper 81-1259, June 1981.

[2]Deese, J. E. and Agarwal, R. K., "Calculation of Axisymmetric Inlet Flowfield Using the Euler Equations," AIAA Paper 83-1853, July 1983.

[3]Jameson, A., "Solution of the Euler Equations for Two-Dimensional Transonic Flow by a Multigrid Method," Paper presented at the International Multigrid Conference, Copper Mountain, CO, April 1983.

[4]Jameson, A. and Baker, T. J., "Solution of the Euler Equations for Complex Configurations," AIAA Paper 83-1929, July 1983.

[5]Baker, T. J., Jameson, A., and Vermeland, R. E., "Three-Dimensional Euler Solutions with Grid Embedding," AIAA Paper 85-121, Jan. 1985.

[6]Swanson, R. C. and Turkel, E., "A Multistage Time-Stepping Scheme for the Navier-Stokes Equations," AIAA Paper 85-35, Jan. 1985.

[7]Agarwal, R. K. and Deese, J. E., "Computation of Transonic Viscous Airfoil, Inlet and Wing Flowfields," AIAA Paper 84-1551, June 1984.

[8]Agarwal, R. K., Underwood, R. R., and Deese, J. E., "Computation of Three-Dimensional Transonic Viscous Flowfields Using Unsteady Parabolized Navier-Stokes Equations," AIAA Paper 85-1595, July 1985.

[9]Baldwin, B. S. and Lomax, H., "Thin Layer Approximation and Algebraic Model for Separated Turbulent Flows," AIAA Paper 78-257, Jan. 1978.

[10]Mehta, U. and Lomax, H., "Reynolds Averaged Navier-Stokes Computations of Transonic Flows: The State-of-the-Art," *Progress in Astronautics and Aeronautics: Transonic Aerodynamics*, Vol. 81, edited by D. Nixon, AIAA, New York, 1981, pp. 297-375.

[11]Thompkins, W. T. Jr., "Analysis of Psuedo-Time-Marching Schemes for Application of Turbomachinery Calculations," *Recent Advances in Numerical Methods in Fluids: Advances in Computational Transonics*, Vol. 4, edited by W. G. Habashi, Pineridge Press, 1985, pp. 577-605.

[12]Lerat, A., "Une classe de schémas aux différences implicites pour les systemes hyperboliques de lois de conservation," *Comptes Rendus Academie des Sciences*, Vol. 288A, 1979, pp. 1033-1036.

[13]Jameson, A., "The Evolution of Computational Methods in Aerodynamics," *Journal of Applied Mechanics*, Vol. 50, 1983, pp. 1052-1070.

[14]Thomas, J. L. and Salas, M. D., "Far-Field Boundary Conditions for Transonic Lifting Solutions to the Euler Equations," AIAA Paper 85-20, Jan. 1985.

[15]Eriksson, L. E., "Transfinite Mesh Generation and Computer-Aided Analysis of Mesh Effects," Ph.D. Thesis, Uppsala University, Uppsala, Sweden, March 1984.

[16]Schmitt, V. and Charpin, F., "Pressure Distributions on the ONERA-M6-Wing at Transonic Mach Numbers," AGARD-AR-138, Chap. B-1, May 1979.

[17]Shang, J. S. and Hankey, W. L. Jr., "Numerical Solution for Supersonic Turbulent Flow Over a Compression Ramp," *AIAA Journal*, Vol. 13, Oct. 1975, pp. 1368-1374.

[18]Visbal, M. and Knight, D., "The Baldwin-Lomax Turbulence Model for Two-Dimensional Shock-Wave/Boundary-Layer Interactions," *AIAA Journal*, Vol. 22, July 1984, pp. 921-928.